UC Irvine
UC Irvine Previously Published Works

Title
Patient-Specific Analysis of Ventricular Vortex Formation and Flow Energetics in Rheumatic and Calcific Mitral Stenosis

Permalink
https://escholarship.org/uc/item/75t8s344

Journal
Annals of Biomedical Engineering

ISSN
0090-6964

Authors
Davey, Marshall
Hashemi, Mohammad Saber
Pressman, Gregg S
et al.

Publication Date
2026-10-09

DOI
10.1007/s10439-026-04364-7

Copyright Information
This work is made available under the terms of a Creative Commons Attribution-NonCommercial-NoDerivatives License, available at https://creativecommons.org/licenses/by-nc-nd/4.0/

Peer reviewed

eScholarship.org Powered by the California Digital Library
University of California

Annals of Biomedical Engineering
https://doi.org/10.1007/s10439-026-04364-7

SI: BIOFLUID MECHANICS AND MECHANOBIOLOGY

Patient-Specific Analysis of Ventricular Vortex Formation and Flow Energetics in Rheumatic and Calcific Mitral Stenosis

Marshall Davey[1] · Mohammad Saber Hashemi[2] · Gregg S. Pressman[3] · Arash Kheradvar[4,5] · Boyce E. Griffith[1,6,7,8,9,10]

Received: 25 April 2026 / Accepted: 26 August 2026
© The Author(s) 2026

Abstract

Purpose Mitral stenosis (MS) accounts for 12% of cardiac patients with single valve disease. There are two main causes: rheumatic disease of the mitral valve (MV) and mitral annular calcification (MAC). While both result in increased transmitral pressure gradients, each has unique effects on valve morphology and pathophysiology. We aimed to study differences in transmitral vortex formation and stroke energetics between the two valve types. We created an *in silico* experimental system using an immersed finite element-finite difference fluid-structure interaction (FSI) scheme and performed three-dimensional flow field analysis.

Materials and Methods Patient-specific, echocardiographic-derived geometries from a healthy MV, a MAC-associated MS valve, and a rheumatic disease-associated MS (RMS) valve were translated into finite element meshes and situated within a left ventricle model driven by a pump-approximating pressure boundary condition at 70 bpm and cardiac outputs of 1.5, 3, 3.5, and 5 L/min over eight cycles.

Results RMS had smaller geometric and effective orifice areas than MAC, but the RMS–MAC differences in mean transmitral pressure gradient and peak transmitral velocity depended on cardiac output. Across equivalent cardiac output conditions, the MAC case required greater pump stroke work and exhibited higher three-dimensional ventricular kinetic energy and viscous energy dissipation than the RMS case. Both diseased cases showed disrupted mitral vortex formation.

Conclusion Three-dimensional FSI simulations suggest that MAC-associated MS may impose a greater energetic burden on ventricular flow than RMS, revealing etiology-specific hemodynamic signatures and providing potential mechanistic insight for improved characterization of MS, warranting further investigation with an expanded valve cohort.

Keywords Mitral stenosis · Mitral annular calcification · Rheumatic mitral stenosis · Transmitral flow · Fluid-structure interaction

Associate Editor Gianni Pedrizzetti oversaw the review of this article.

✉ Arash Kheradvar
arashkh@uci.edu

✉ Boyce E. Griffith
boyceg@email.unc.edu

1 Department of Mathematics, University of North Carolina at Chapel Hill, Chapel Hill, NC, USA

2 Mike Wiegers Department of Electrical and Computer Engineering, Kansas State University, Manhattan, KS, USA

3 Division of Cardiology, Heart and Vascular Institute, Jefferson Einstein Medical Center, Thomas Jefferson University, Philadelphia, PA, USA

4 Department of Biomedical Engineering, University of California, Irvine, CA, USA

5 Department of Radiological Sciences, University of California, Irvine, CA, USA

6 Department of Biomedical Engineering, University of North Carolina at Chapel Hill, Chapel Hill, NC, USA

7 Department of Applied Physical Sciences, University of North Carolina at Chapel Hill, Chapel Hill, NC, USA

8 Carolina Center for Interdisciplinary Applied Mathematics, University of North Carolina at Chapel Hill, Chapel Hill, NC, USA

9 Computational Medicine Program, University of North Carolina School of Medicine, Chapel Hill, NC, USA

10 McAllister Heart Institute, University of North Carolina School of Medicine, Chapel Hill, NC, USA

Published online: 09 October 2026

Introduction

Mitral stenosis (MS) accounts for approximately 12% of patients with heart valve disease involving only a single valve [1]. Historically, rheumatic mitral stenosis (RMS) has been the predominant cause worldwide, but in aging populations, particularly in high-income countries, mitral annular calcification (MAC) has emerged as an increasingly common etiology. In a large U.S. echocardiographic cohort, MAC was identified in 23% of patients undergoing imaging, and MS was present in 6.6% of patients with MAC compared with only 0.5% of individuals without annular calcification [2]. Importantly, the prognosis of MS—particularly when associated with MAC—is poor, with reported five-year survival rates below 50% [3].

Rheumatic valvular disease is the result of repeated group A streptococcal infections. Molecular mimicry between streptococcal antigens and human valve proteins allows antistreptococcal antibodies to cross-react with valve tissue resulting in leaflet fibrosis and fusion of the valve commissures [4]. This produces a "funnel"-shaped geometry, with the greatest stenosis occurring at the leaflet tips. MAC, in contrast, is an inflammatory disease of uncertain etiology whose chief risk factors are advanced age and chronic kidney disease. Calcium deposits accumulate within the fibrous annulus supporting the mitral valve, and may extend onto the leaflet bases, restricting leaflet motion. In severe cases, a calcific "tunnel" forms that produces valvular stenosis. Unlike RMS, the minimum flow area for blood flow in MAC-associated MS is located near the annulus rather than at the leaflet tips. Furthermore, the valve apparatus (from the annulus to the leaflet tips) is typically smaller in MAC-associated MS than in RMS, giving the valve a shrunken appearance [5]. Representative echocardiographic images illustrating these distinct disease morphologies are provided in Fig. 1.

These structural differences have important implications for ventricular inflow dynamics, which are not adequately captured by traditional Doppler echocardiographic measures (e.g., transmitral pressure gradients, valve area, and Doppler flow velocities). In MAC, the altered geometry can disrupt normal transmitral vortex formation and has been associated with increased vortex formation time [6] as well as elevated viscous energy dissipation measured *in vitro* [7], suggesting a reduction in cardiac efficiency. Despite these observations, the mechanisms by which these distinct etiologies alter ventricular flow organization remain understudied.

Normal ventricular filling is characterized by the formation of a coherent diastolic vortex ring that facilitates efficient transport of blood from the mitral valve toward the left ventricular outflow tract during systole [8–11]. This vortex structure plays an important role in momentum transfer, ventricular washout, and minimization of energy loss within the ventricle. Disruption of vortex formation can therefore impair ventricular efficiency and increase energetic losses. Clinical imaging modalities, however, have limited ability to characterize these flow structures in detail [12]. Doppler echocardiography measures velocities only along the ultrasound beam direction and therefore cannot reconstruct the full three-dimensional velocity field within the ventricle. Even advanced imaging techniques such as four-dimensional flow magnetic resonance imaging provide limited spatial and temporal resolution for resolving fine-scale vortical structures and shear layers responsible for viscous energy dissipation. Consequently, clinically derived hemodynamic metrics may not fully capture the energetic consequences of altered ventricular flow patterns in MS.

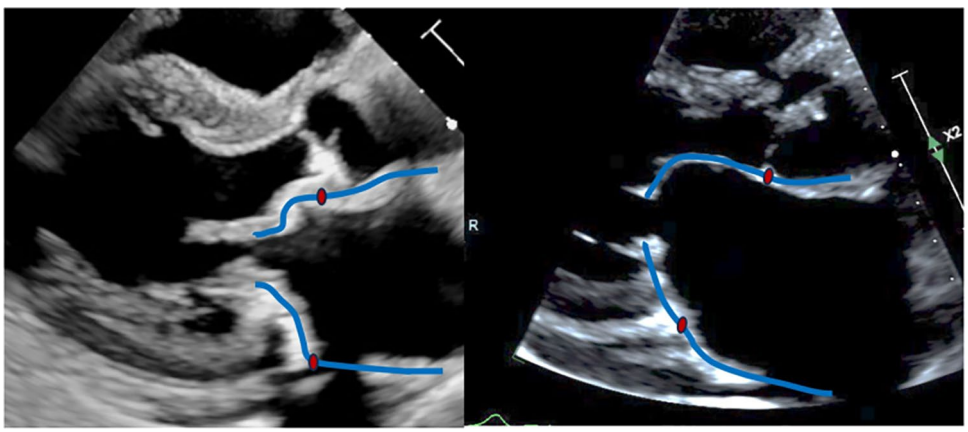


Fig. 1 Echocardiographic images (parasternal long-axis view) of patients with mitral stenosis due to MAC (left) and rheumatic disease (right) [57]. The anterior mitral leaflet is on top in each case. The description of MAC as "tunnel"-like comes from the calcific restriction close to the mitral annulus (the red dots; the blue lines define the leaflets, to the left of the annulus, and the left atrial walls, to the right of the annulus). The "funnel"-like description of RMS relates to the leaflet restriction occurring toward the leaflet tips and away from the mitral annulus. Reproduced with permission from Faggiano et al. [57]

Experimental investigations have begun to address these limitations by measuring intraventricular flow fields using particle image velocimetry (PIV). A limited number of *in vitro* studies have examined the hemodynamic effects of MS and interventions [5, 7, 13–17], with only two directly comparing RMS and MAC-associated MS [5, 13]. Gilon *et al*. demonstrated reduced orifice-adjusted transmitral pressure gradients in RMS relative to MAC-associated MS [13], whereas Hashemi *et al*. reported higher kinetic energy and viscous energy dissipation in MAC-associated MS [5]. Although these studies provided important insights, only two incorporated reconstructions of ventricular flow fields [5, 7], and their flow energetic analyses were limited to two-dimensional velocity measurements obtained from planar PIV measurements. Because ventricular flow is inherently three-dimensional, planar measurements may substantially underestimate true intraventricular energy dissipation and fail to capture complex vortex interactions throughout the cardiac cycle.

Computational modeling offers a complementary approach capable of overcoming many of these experimental and clinical limitations. Existing *in silico* studies of MS have primarily employed simplified lumped-parameter circulatory models in which the mitral valve is represented by scalar orifice parameters [18, 19]. Although these models can reproduce global hemodynamic trends, they lack the spatial resolution necessary to resolve ventricular vortex formation, complex flow interactions, and the associated energetic losses. High-fidelity fluid–structure interaction (FSI) simulations provide an opportunity to investigate these mechanisms in greater detail by resolving the full three-dimensional velocity field and the dynamic interaction between blood flow, ventricular geometry, and valve motion. The importance of FSI has been highlighted especially for cyclic loading conditions, such as from the cardiac cycle [20].

Several left ventricular (LV) FSI models have been reported in the literature based on smoothed-particle hydrodynamics (SPH) methods [21–23], arbitrary Lagrangian–Eulerian methods [24–27], and immersed boundary methods [28–32]. Most of these models were developed to reproduce healthy *in vivo* dynamics using patient-derived LV geometries, and, for computational efficiency, often exclude one or both cardiac valves. Nevertheless, several of these FSI studies have been extended to investigate disease-specific alterations in ventricular hemodynamics, including chordal rupture and repair [21, 22], impaired LV relaxation [31], systemic circulation stenosis and hypertension [29], and ischemic mitral regurgitation [24]. To the best of our knowledge, however, no patient-specific LV FSI studies have specifically investigated the impact of MS on intraventricular flow patterns and flow energetics.

There is a critical need for quantitative studies that directly compare ventricular flow features and energetic consequences in RMS vs. MAC-associated MS using three-dimensional flow velocity data. Such analyses could uncover etiology-specific hemodynamic signatures not captured by conventional clinical metrics, improving mechanistic understanding of disease severity and treatment outcomes. This gap is especially important given the rising prevalence of degenerative MS in aging populations and the limited mechanistic evidence guiding emerging interventional therapies.

In this study, we investigate the effects of mitral stenosis on left ventricular flow energetics using an *in silico* experimental design based on the *in vitro* work of Hashemi *et al*. [5] (Fig. 2). Through this framework, we aim to identify mechanistic differences in ventricular hemodynamics between RMS and MAC-associated MS and provide new insights into the energetic consequences of these distinct disease etiologies.

Materials and Methods

Experimental Platform

The computational domain geometry is derived from a previously published *in vitro* heart flow simulator used for the investigation of MS using PIV [5]. In that experimental platform, patient-specific mitral valve geometries reconstructed from three-dimensional transesophageal echocardiography were fabricated as silicone models and mounted within a modular left heart simulator [33, 34]. The mitral valve was placed within a rigid atrial chamber, whereas a compliant, transparent silicone left ventricular (LV) sac was suspended within a water-filled enclosure, allowing optical access for flow visualization. A bioprosthetic aortic valve (AV) was positioned in the LV outflow tract to complete the left heart configuration. The test setup is shown in Fig. 2.

Blood and Circulation Modeling

In the *in vitro* system, cardiac pulse was generated using a programmable pulse duplicator system (ViVitro SuperPump, Victoria, BC), which actuated cyclic expansion and contraction of the LV sac to reproduce physiologic filling and ejection dynamics. The system was operated at a fixed heart rate of 70 beats per minute using the standardized FDA waveform, with cardiac output (CO) conditions constrained by the experimental setup (nominally up to ~ 3.5 L/min). This configuration enabled controlled, repeatable transmitral flow conditions while minimizing confounding effects of native chamber compliance and physiologic variability. The pump action *in silico* was modeled using a prescribed flow rate-informed pressure boundary condition at the bottom of the domain modeled on the same FDA waveform. Simulations were run at a variety of cardiac outputs (1.5, 3.0, 3.5, 5.0 L/

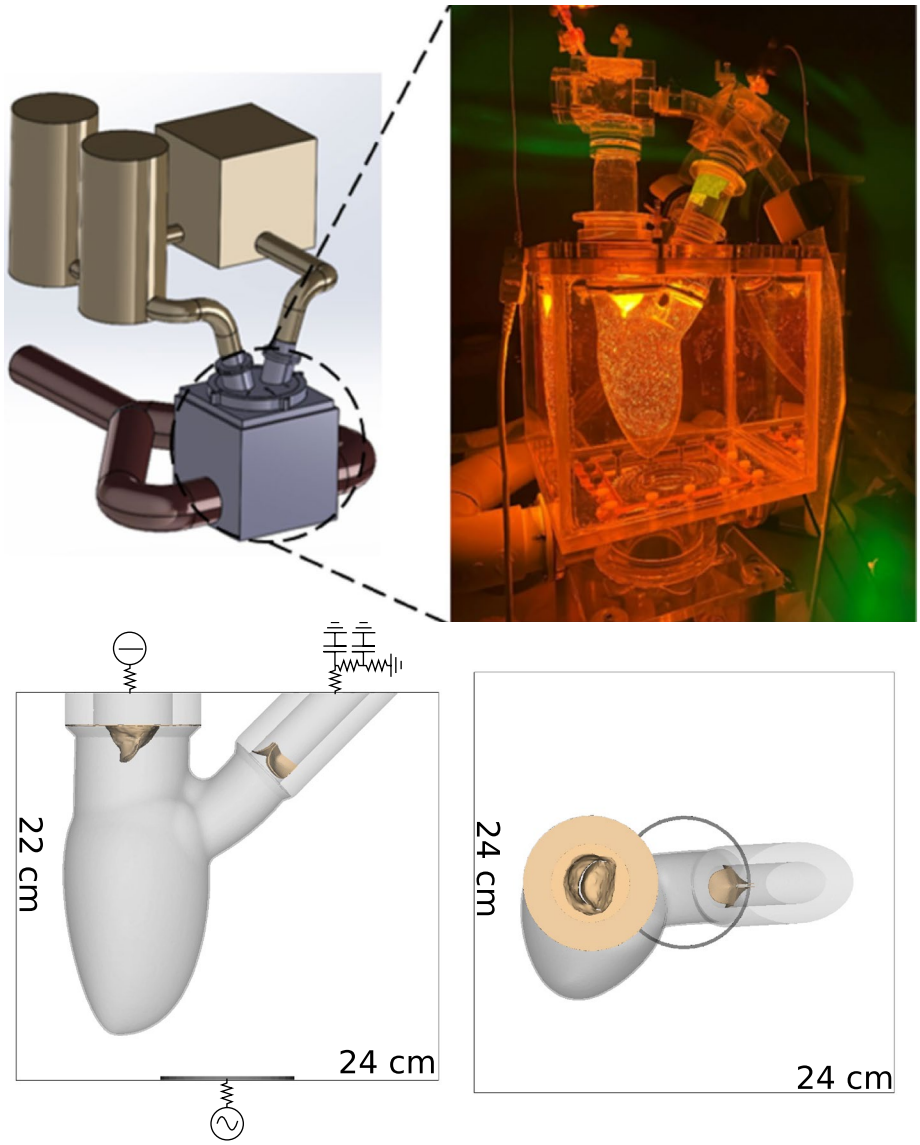


Fig. 2 Lateral (bottom, left) and atrial-ventricular (bottom, right) views of the computational domain with the representative NHC valve. The x-axis is the bottom in each figure. The dimensions of each side have been included for perspective. The lateral view includes the 0-dimensional circulation models at the pump port and the inflow/outflow of the ventricle that were adapted from previous *in vitro* experimental setups [5, 34]. An illustration of the full *in vitro* system (top, left) as well as a photo of the test chamber (top, right) are included for reference [5]. The upper panels are reproduced with permission from Hashemi et al. [5]

min) to observe any changes related to flow rate variations. The higher cardiac output values encompass both reduced cardiac output (3.0 and 3.5 L/min) and a physiologically normal condition (5.0 L/min) for an adult heart. In contrast, a cardiac output of 1.5 L/min is incompatible with sustained physiologic function and was therefore considered an intentionally non-physiologic condition. Simulations at this flow rate were included solely to obtain cases with Reynolds numbers below the thresholds for transition to turbulence and fully turbulent flow, thereby enabling comparison across distinct flow regimes. A more comprehensive description of how the action of the pump was captured *in silico* is included in supplemental section **A. Pressure Driven Ventricular Flow**.

Upstream and downstream hemodynamic conditions *in vitro* were regulated through the intrinsic compliance of the atrial and ventricular components of the simulator rather than discrete lumped chambers, allowing physiologic pressure–flow coupling across the valve. In the corresponding *in silico* model, these effects are represented using reduced order models that specify the boundary conditions. We used a constant 10 mmHg pressure boundary condition upstream of the MV, and the outflow boundary condition was modeled using a mix of grounded compliance chambers and resistances. The pressure boundary condition of 10 mmHg was chosen to approximate the pressure in the left atrium, and pressure measurements in the *in vitro* work were not available. Fig. 2 illustrates the reduced order boundary models. The portions of the boundary not described by reduced order models were treated with zero-velocity boundary conditions to ensure the pump would drive the cardiac cycle within the LV.

Flow field measurements in the *in vitro* system were obtained using 2D PIV, with the LV illuminated by a laser

sheet and seeded particles tracked at high temporal resolution (~1 kHz) to resolve transient intraventricular flow structures [5]. Notably, the working fluid in the experimental setup was water to ensure optical transparency and compatibility with PIV. To replicate the *in vitro* work and physiologic hemodynamics *in silico*, the fluid was modeled as incompressible and Newtonian with a density of 1,000 kg/m^3. In the majority of the simulations, we used a dynamic viscosity of 4.0 mPa·s, approximating blood's properties at the organ scale [35] in contrast to the *in vitro* work, but we ran additional simulations at 1.0 mPa·s to recreate the *in vitro* experimental design that used water as the test fluid. The blood analog was modeled as an incompressible, Newtonian fluid. This assumption was adopted to match the Newtonian test fluid used in the *in vitro* experiments and is consistent with the standard approach used in organ scale FSI models of LV hemodynamics [22, 26, 28].

Ventricle and Mitral Valve Modeling

The left ventricular geometry used in the computational model was constructed from the silicone LV sac geometry and subsequently processed to generate a volumetric finite element representation. The LV wall was assigned a uniform thickness (1 mm) and discretized using a tetrahedral mesh generated via fTetWild [36]. To ensure consistency with the mechanical response of the *in vitro* model, the structural material behavior was parameterized using manufacturer-provided stress–strain data for the silicone material.

We used three anonymized mitral valve geometries: an RMS case, a MAC-associated MS case, and a healthy MV, or normal healthy case (NHC) (Fig. 3). The valve geometries were digitally extracted from 4D-echocardiography data at the onset of systole when the mitral leaflets are just touching [7]. The digital valve geometries were processed directly for the *in silico* experiments, and the valve surfaces were digitally thickened to 1 mm. The constitutive material parameters were derived from a previous stress-strain study on Smooth-On Dragonskin 10 [37], as this material was used to fabricate the patient-specific MVs for the *in vitro* experiments. In the MAC-associated MS case, an additional calcific ring geometry was also generated from the 4D-echocardiography images and treated as rigid *in silico* as it was a rigid plastic *in vitro*. Table 1 includes summary geometric statistics for each valve model. The orifice area was geometrically extracted during the maximal valve opening in a similar manner to 3D echocardiographic planimetry. The bioprosthetic AV geometry and material model was adopted from previous *in vitro-in silico* valve studies [38, 39].

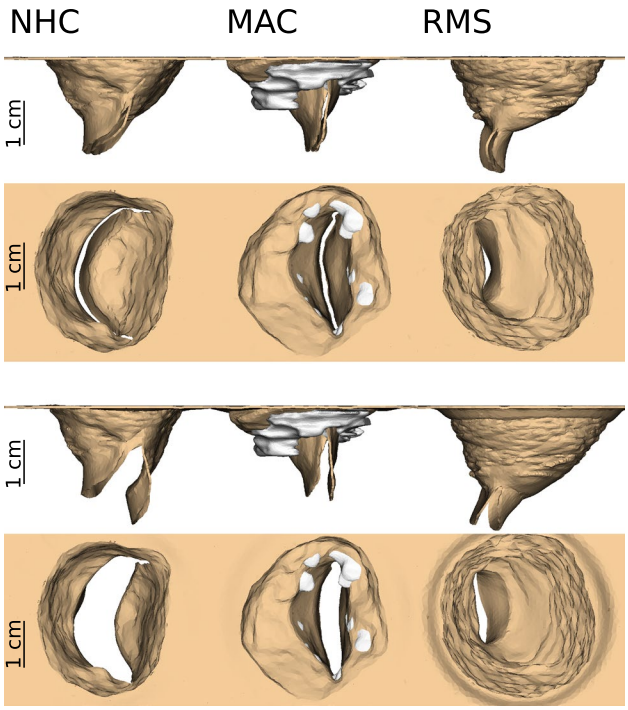


Fig. 3 The representative valve geometries including the calcification in the MAC disease case. The posterior leaflets are on the left in both the lateral and atrial-ventricular views. Valves are shown in the initial position (rows 1, 2) and while maximally open during diastole (rows 3, 4). Scales are consistent across each image in a row

Fluid-Structure Interaction Modeling

The computational model was based on the IBAMR fluid-structure interaction software package with finite element structural representations immersed within a Cartesian domain with adaptive mesh refinement [40–44]. IBAMR uses SAMRAI [45] for Cartesian background grid handling and PETSc for linear solver infrastructure [46–48]. The finite element infrastructure was handled with deal.II [49–51]. This software package was chosen because of past studies of *in vitro* systems for bioprosthetic AVs [38, 39, 52, 53] and whole heart simulation [54].

Results

Simulations were performed over eight consecutive cardiac cycles, with data from the first three cycles discarded to allow transient effects to decay and the solution to approach a periodic steady state with respect to bulk flow metrics. The remaining five cycles were used for statistical analysis, providing sufficient samples to achieve a statistical power of approximately 0.8 at $p < 0.05$ [55]. The reported average values with the corresponding single standard deviations were computed from the remaining five cycles. Cross valve

comparisons were evaluated using the one-sided Mann-Whitney U test, and the p-values are reported in parentheses. Further discussion on the convergence of the time series bulk flow metrics is included in supplemental section **B. Bulk Flow Metric Convergence**.

The cardiac output values considered were 1.5 L/min (non-physiologic CO, sub-transition to turbulent flow Reynolds number), 3.0 L/min (reduced CO), 3.5 L/min (reduced CO), and 5.0 L/min (healthy CO). A simulation series with each valve was run at 3.5 L/min with water for direct comparison with the *in vitro* work. The NHC valve fully inverted during the 5.0 L/min simulation, so there is not an NHC comparison at that flow rate.

Transmitral Pressure Gradient and Maximum Velocity

A common diagnostic metric for MS is the transmitral pressure gradient. We computed the transmitral pressure gradient in a manner like catheter derived values [7] by taking the difference in the local pressure upstream of the MV and at the LV centroid. The LV pressure is computed from the simulated pressure field by extracting the mean value within a 2 mm radius sphere located at the geometric centroid of the LV. The time series data for the MV gradient is included as Fig. 4b, and the maximum and mean gradient values are reported in Table 2. The maximum and mean gradients are elevated in both the RMS and MAC-associated MS cases as compared to the NHC for all COs with a NHC comparison ($p < 5e{-}3$). The mean transmitral pressure gradient is elevated in the RMS case as compared to the MAC case as well for COs 1.5 and 3.0 L/min ($p < 5e{-}3$), but the mean gradient is not significantly different between the two diseased valves for COs of 5.0 L/min and 3.5 L/min with blood analog and water ($p > 0.05$). The maximum transmitral pressure gradient is not statistically different between the two diseased cases for the CO of 3.0 L/min and 3.5 L/min with water and blood analog ($p > 0.1$), but the maximum pressure gradient is significantly larger for MAC than for RMS at 5.0 L/min ($p < 5e{-}3$). Between the 3.5 L/min cases, the maximum gradient is consistently lower with water ($p < 0.01$), and the mean gradient is reduced in the diseased cases with water ($p < 0.03$).

We then computed the maximum velocity across each valve during the E wave and A wave of the diastolic phase (Table 2). The maximum velocity is largest for the RMS valve for all COs ($p < 5e{-}3$) except for 5.0 L/min, where the maximum velocity for MAC is larger ($p < 5e{-}3$). The NHC valve consistently has the smallest maximum velocity ($p < 5e{-}3$). For the 3.5 L/min cases, the water simulations have a consistently lower maximum velocity ($p < 0.01$) in the disease cases but no statistical difference for the NHC valve. From the maximum velocity and the concurrent flow rate through the MV, we compute the effective orifice area (EOA) (Table 3) assuming plug flow, which is consistent methodologically with the *in vitro* work [5]. Across all CO conditions, the NHC has the largest EOA ($p < 5e{-}3$), and the RMS case has the smallest EOA ($p < 5e{-}3$). The EOA is not significantly different ($p > 0.1$) between water and blood analog with any valve in the 3.5 L/min cases. For the simulations with blood analog, the EOA does not increase significantly across successive CO increases ($p > 0.1$) for any valve, except for the change from 1.5 L/min to 3.0 L/min ($p < 5e{-}3$).

The coefficient of contraction (CoC) (Table 3) was then computed using the geometric orifice areas stated in Table 1. The CoC is significantly larger in the NHC than the diseased cases ($p < 5e{-}3$) across all COs over 1.5 L/min; at 1.5 L/min none are significantly different. Similarly, across all COs over 1.5 L/min, the CoC for the RMS case is larger than the MAC case ($p < 0.03$). The CoC is not significantly different ($p > 0.1$) between water and blood analog with any valve in the 3.5 L/min cases. For the simulations with blood analog, the CoC does not increase significantly across successive CO increases ($p > 0.1$) for each valve, except for the change from 1.5 L/min to 3.0 L/min ($p < 5e{-}3$).

The Reynolds number consistently increases with CO ($p < 5e{-}3$) with the same valve, and water has a higher Reynolds number than blood analog at 3.5 L/min ($p < 5e{-}3$). The NHC valve Reynolds number is consistently smaller than the Reynolds number for the MAC-associated MS valve ($p < 0.03$) across all cases, and the Reynolds number for the NHC valve is smaller than that of the RMS valve for the 3.5 L/min cases. The MAC valve produces a larger Reynolds number at 3.5 L/min and 5.0 L/min with blood analog ($p < 0.01$), but the values are not significantly different ($p > 0.4$) with water at 3.5 L/min. The Reynolds number for each valve with blood analog is in the transition between laminar flow and turbulent flow for the CO of 3 L/min and 3.5 L/min, with the turbulent regime fully realized at 5.0 L/min for both diseased valves. The water cases are all within the turbulent regime.

Table 1 Estimated geometric values for the mitral valves during maximal valve opening during diastole

Valve	NHC	MAC	RMS
Orifice Area (cm^2)	2.4	1.42	0.87
Leaflet Gap (cm)	1.16	0.68	0.4
Posterior Bias (^{o})	1.6	−10	49

The leaflet gap and posterior bias are based on the mitral jet during E wave extracted from the plane slice bisecting the mitral and aortic valves. The posterior bias reflects how much the mitral jet is deflected toward the posterior leaflet and lateral wall. A bias of 0° indicates the mitral jet is directed straight down into the ventricle

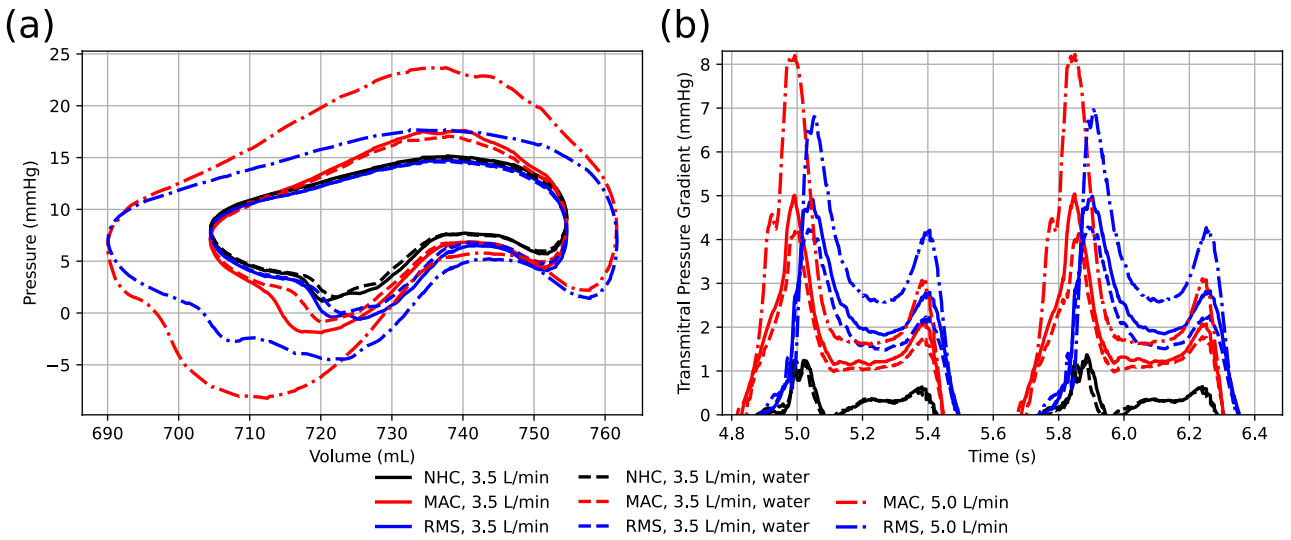


Fig. 4 **a** The ventricular pressure–volume relations over the final two cycles used to compute the pump stroke work for the 3.5 L/min and 5.0 L/min simulations. **b** The transmitral pressure gradient data during diastole over the final two cycles for the 3.5 L/min and 5.0 L/min simulations. Summary statistics are included in Table 2 and Table 4

Table 2 Averages and standard deviations over the last five cycles of the maximum and mean gradients across the mitral valves with maximum E wave and A wave velocities

Case	Max gradient (mmHg)	Mean gradient (mmHg)	Max E wave velocity(cm/s)	Max A wave velocity (cm/s)
N, 1.5 L/min	0.4975 ± 6.8e−2	0.1493 ± 1.0e−2	38.08 ± 3.2	29.61 ± 0.67
M, 1.5 L/min	1.435 ± 2.1e−2	0.7046 ± 2.2e−2	58.76 ± 0.45	47.72 ± 0.87
R, 1.5 L/min	1.596 ± 9.9e−2	0.8175 ± 4.2e−2	67.07 ± 2.0	53.03 ± 1.8
N, 3.0 L/min	1.087 ± 2.8e−2	0.3034 ± 1.7e−2	65.05 ± 4.7	46.98 ± 2.2
M, 3.0 L/min	3.874 ± 3.6e−2	1.455 ± 3.0e−2	108.4 ± 3.6	67.46 ± 0.83
R, 3.0 L/min	3.954 ± 0.18	1.769 ± 8.5e−2	124.9 ± 4.0	81.80 ± 1.6
N, 3.5 L/min	1.336 ± 6.3e−2	0.3451 ± 2.0e−2	69.94 ± 6.1	46.60 ± 3.5
M, 3.5 L/min	5.007 ± 3.3e−2	1.792 ± 3.0e−2	139.2 ± 4.0	74.29 ± 2.1
R, 3.5 L/min	4.804 ± 0.27	2.035 ± 0.18	144.5 ± 5.0	91.58 ± 2.3
Nw, 3.5 L/min	1.221 ± 2.1e−2	0.3244 ± 1.7e−2	70.20 ± 6.3	46.60 ± 3.0
Mw, 3.5 L/min	4.178 ± 7.0e−2	1.498 ± 2.7e−2	119.1 ± 4.4	70.46 ± 3.5
Rw, 3.5 L/min	4.181 ± 0.15	1.719 ± 0.16	132.9 ± 3.0	81.83 ± 2.3
M, 5.0 L/min	8.191 ± 6.9e−2	2.917 ± 3.9e−2	184.5 ± 7.4	96.58 ± 2.8
R, 5.0 L/min	6.649 ± 0.43	2.734 ± 0.20	168.0 ± 2.6	114.2 ± 0.88

N = NHC, M = MAC case, R = RMS case, w = simulation with water rather than blood dynamic viscosity

From the computed LV pressures used to generate the MV pressure gradients and the flow rates measured at the LV inlet and outlet, we estimated the work required by the pump-approximating boundary condition to maintain the prescribed stroke volumes within the LV, which we refer to as the pump stroke work (Table 4), by computing the inscribed areas of the LV pressure–volume relations (Fig. 4a). Despite the larger MV gradient and velocities in the RMS valve, the MAC case produced the largest pump stroke work ($p < 5e{-}3$), and the NHC case produced the lowest pump stroke work estimate, as anticipated ($p < 5e{-}3$). The pump stroke work increased with CO ($p < 5e{-}3$), and the pump stroke work was smaller for the 3.5 L/min case with water than with blood analog for all valve geometries ($p < 5e{-}3$).

Kinetic Energy and Viscous Energy Dissipation Rate

As the pump stroke work values suggested a difference in the energetics between the different valve models, the kinetic energy and viscous energy dissipation rate densities were computed within the LV model [7, 56]. Planar energies and

Table 3 Estimated average effective orifice area, coefficient of contraction, and Reynolds number with standard deviations across the final five cycles. From Table 1, the geometric orifice areas are 2.4 cm^2 for the NHC valve, 1.42 cm^2 for the MAC valve, and 0.87 cm^2 for the RMS valve

Case	Effective orifice area (cm^2)	Coefficient of contraction	Reynolds number
N, 1.5 L/min	0.9962 ± 0.15	0.4151 ± 0.063	1070 ± 124
M, 1.5 L/min	0.6461 ± 0.13	0.4550 ± 0.090	1327 ± 134
R, 1.5 L/min	0.4008 ± 0.021	0.4606 ± 0.024	1198 ± 55
N, 3.0 L/min	1.987 ± 0.11	0.8280 ± 0.046	2581 ± 118
M, 3.0 L/min	0.7988 ± 0.066	0.5626 ± 0.047	2733 ± 185
R, 3.0 L/min	0.5688 ± 0.050	0.6538 ± 0.057	2658 ± 194
N, 3.5 L/min	2.250 ± 0.18	0.9375 ± 0.073	2947 ± 142
M, 3.5 L/min	0.8806 ± 0.081	0.6201 ± 0.057	3680 ± 177
R, 3.5 L/min	0.6174 ± 0.048	0.7096 ± 0.055	3203 ± 217
Nw, 3.5 L/min	2.054 ± 0.18	0.8560 ± 0.073	11300 ± 556
Mw, 3.5 L/min	0.8768 ± 0.11	0.6174 ± 0.074	12540 ± 518
Rw, 3.5 L/min	0.6104 ± 0.050	0.7016 ± 0.058	11710 ± 625
M, 5.0 L/min	0.9664 ± 0.12	0.6806 ± 0.081	5100 ± 255
R, 5.0 L/min	0.6847 ± 0.051	0.7870 ± 0.059	3916 ± 114

N = NHC, M = MAC, R = RMS, w = simulation with water rather than blood dynamic viscosity

three-dimensional energies were computed. The plane slice used for the two-dimensional computations bisected each MV and the AV akin to planar PIV used in previous experiments [5, 7] and was consistent across each valve and CO. The energy values were computed using weighted area and volume sums for the planar and three-dimensional values, respectively, which were regularized by the respective total areas and volumes to create a density. The areas and volumes correspond to the Cartesian cells contained within the ventricle. The time series data for the energetics are included as Fig. 5, and the maximum and mean values are summarized in Tables 5-8.

The planar kinetic energy values (Fig. 5a, Table 5) and viscous energy dissipation rate values (Fig. 5b, Table 6) support the findings of the pump stroke work, in that the energies are lowest in the NHC valve ($p < 5e{-}3$) and largest in the MAC case ($p < 5e{-}3$), and the planar energies increase with CO for all valves ($p < 5e{-}3$). The exception is the comparison of the maximum planar dissipation rate values for the MAC case and the RMS case for 1.5 L/min and 3.5 L/min with water, where the maximum differences are not statistically different ($p > 0.1$). The average planar dissipation rates also do not differ significantly between MAC and RMS at 1.5 L/min. Water at 3.5 L/min, compared

Table 4 Average pump stroke work, stroke volume, ejection fraction, end-diastolic volume, and end-systolic volume over the last five cycles with the corresponding standard deviations. Stroke work was computed from the areas circumscribed by the pressure–volume relations. The initial volume of the left ventricle model is 783.1 mL

Case	Pump stroke work (mJ)	Stroke volume (mL)	Ejection fraction (%)	End-diastolic volume (mL)	End-systolic volume (mL)
N, 1.5 L/min	8.656 ± 0.1212	21.48 ± 3.2e−4	2.883 ± 1.2e−4	745.2 ± 4.4e−2	723.7 ± 4.3e−2
M, 1.5 L/min	10.34 ± 0.1055	21.48 ± 3.0e−4	2.883 ± 1.2e−4	745.1 ± 4.1e−2	723.7 ± 4.1e−2
R, 1.5 L/min	9.7535 ± 0.04906	21.48 ± 3.5e−4	2.883 ± 1.2e−4	745.2 ± 4.4e−2	723.7 ± 4.3e−2
N, 3.0 L/min	38.89 ± 0.05913	42.96 ± 3.5e−4	5.712 ± 5.9e−4	752.2 ± 8.4e−2	709.2 ± 8.4e−2
M, 3.0 L/min	50.39 ± 0.2455	42.97 ± 5.3e−4	5.713 ± 5.3e−4	752.2 ± 7.8e−2	709.2 ± 7.8e−2
R, 3.0 L/min	43.74 ± 0.3524	42.96 ± 6.0e−4	5.712 ± 5.6e−4	752.2 ± 8.4e−2	709.2 ± 8.3e−2
N, 3.5 L/min	54.43 ± 0.1499	50.13 ± 7.2e−4	6.643 ± 7.6e−4	754.5 ± 9.7e−2	704.4 ± 9.7e−2
M, 3.5 L/min	74.27 ± 0.3618	50.13 ± 2.7e−4	6.644 ± 7.6e−4	754.5 ± 9.1e−2	704.4 ± 9.0e−2
R, 3.5 L/min	61.14 ± 0.5618	50.12 ± 8.3e−4	6.643 ± 7.5e−4	754.5 ± 9.7e−2	704.4 ± 9.6e−2
Nw, 3.5 L/min	52.27 ± 0.05917	50.13 ± 8.1e−4	6.643 ± 7.6e−4	754.5 ± 9.8e−2	704.4 ± 9.7e−2
Mw, 3.5 L/min	67.85 ± 0.5041	50.13 ± 4.0e−4	6.644 ± 7.6e−4	754.5 ± 9.2e−2	704.4 ± 9.2e−2
Rw, 3.5 L/min	57.64 ± 0.4948	50.12 ± 7.8e−4	6.643 ± 7.5e−4	754.5 ± 9.8e−2	704.4 ± 9.7e−2
M, 5.0 L/min	175.1 ± 0.3385	71.61 ± 7.8e−4	9.403 ± 1.4e−4	761.5 ± 0.13	689.9 ± 0.13
R, 5.0 L/min	132.9 ± 1.022	71.60 ± 7.4e−4	9.402 ± 1.6e−4	761.6 ± 0.14	689.9 ± 0.14

N = NHC, M = MAC case, R = RMS case, w = simulation with water rather than blood dynamic viscosity

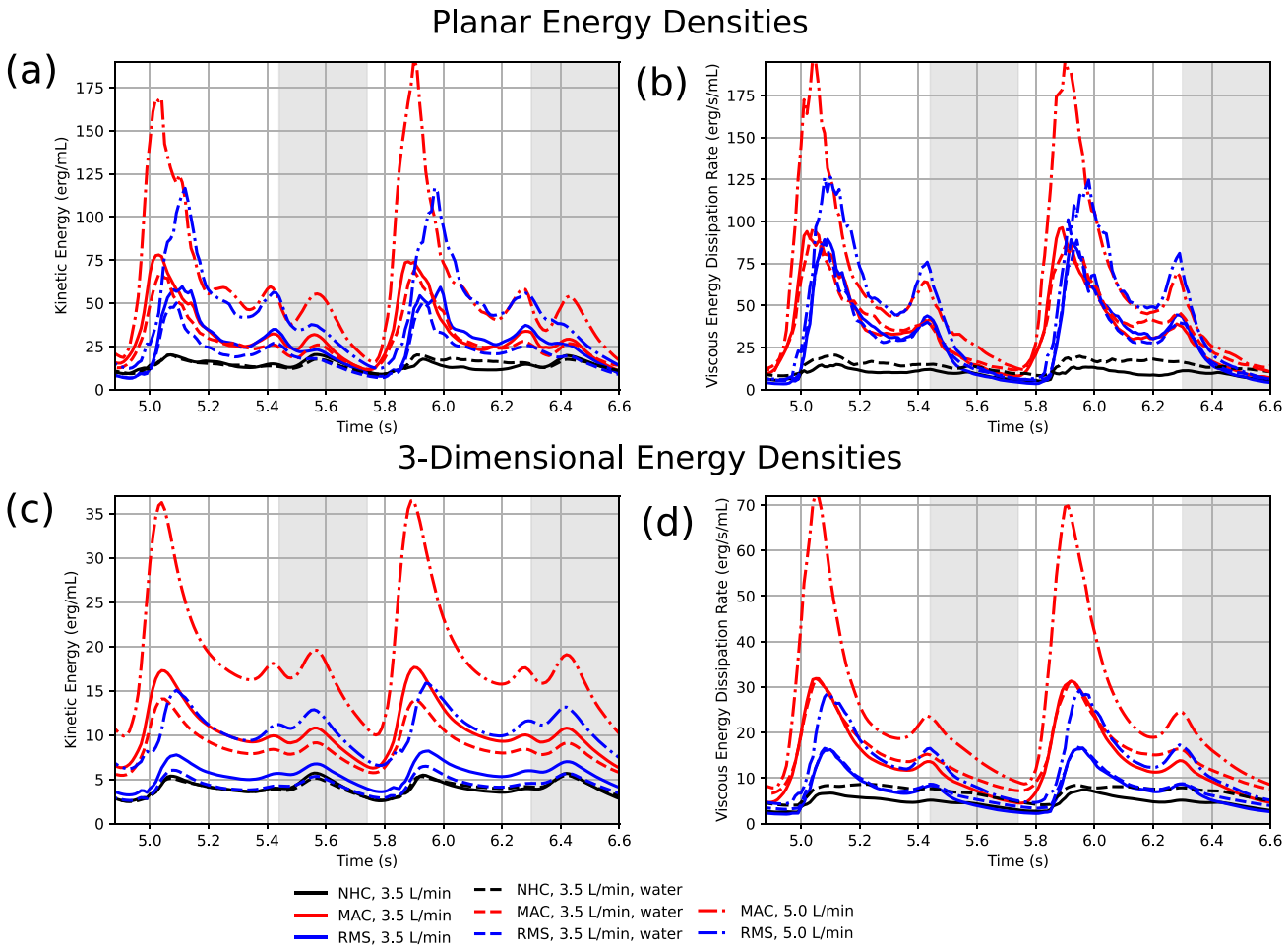


Fig. 5 Planar kinetic energy (**a**) and viscous energy dissipation rate (**b**) estimates compared to full three-dimensional calculations of kinetic energy (**c**) and viscous energy dissipation rate **(d)** over the final two cycles within the ventricle. The systolic phases of the cycles are highlighted with gray for clarity in all figures

to the blood analog, has reduced total planar kinetic energy in the diseased cases ($p<0.03$) and reduced maximum planar kinetic energy for all valves ($p<0.05$). For the planar viscous energy dissipation rate differences between water and blood analog, water produces higher cumulative and maximum dissipation rates ($p<5e{-}3$) in the NHC valve, and there is more planar dissipation during systole for all valves with water ($p<0.03$).

The three-dimensional kinetic energy values (Fig. 5c, Table 7) and viscous energy dissipation rate values (Fig. 5d, Table 8) support the findings of the pump stroke work and the planar energies, in that the energies are largest in the MAC case ($p<5e{-}3$), and the energies increase with CO across all valves ($p<5e{-}3$). There is a marked difference in the three-dimensional and planar viscous energy dissipation rates of the MS cases. In the three-dimensional analysis, the MAC energy dissipation rates are significantly larger than the RMS values for both the maximum and average dissipation rates ($p<5e{-}3$) across all equivalent CO comparisons. In contrast, the planar analysis showed no statistically significant difference between the maximum dissipation rates for the RMS and MAC-associated MS cases at 3.5 L/min with water and 1.5 L/min, or between the average dissipation rates at 1.5 L/min. This discrepancy is most likely attributable to the reduced out-of-plane velocities (defined by the plane that bisects the MV and AV) observed in the RMS case across all valve configurations (Fig. S8). Water at 3.5 L/min, compared to blood analog, has reduced total kinetic energy in the diseased cases ($p<0.03$) and reduced maximum kinetic energy for all valves ($p<0.03$). As with the planar dissipation, the significant differences in the viscous energy dissipation rate between water and blood analog are that water produces higher cumulative and maximum dissipation rates ($p<0.02$) in the NHC valve, cumulative dissipation rate over the entire cycle in the MAC case is increased with water ($p<0.02$), and cumulative dissipation over systole is increased with water across all valves ($p<0.03$).

Table 5 Average planar kinetic energy time integrals and max value during respective parts of the cycle with standard deviation over the last five consecutive cycles. The velocity normal to the plane was excluded

Case	Total (erg˙s/mL)	Diastole (erg˙s/mL)	Systole (erg˙s/mL)	Max (erg/mL)
N, 1.5 L/min	3.189 ± 0.17	2.023 ± 0.15	1.166 ± 0.040	4.990 ± 0.14
M, 1.5 L/min	8.258 ± 0.92	5.733 ± 0.66	2.525 ± 0.28	15.00 ± 1.6
R, 1.5 L/min	5.438 ± 0.62	3.569 ± 0.53	1.869 ± 0.088	9.031 ± 1.2
N, 3.0 L/min	9.155 ± 1.4	5.651 ± 1.0	3.503 ± 0.38	15.73 ± 1.4
M, 3.0 L/min	24.45 ± 1.5	17.99 ± 1.4	6.464 ± 0.34	57.23 ± 3.2
R, 3.0 L/min	16.02 ± 1.7	11.40 ± 1.7	4.624 ± 0.21	37.13 ± 4.7
N, 3.5 L/min	11.92 ± 0.98	7.426 ± 0.86	4.491 ± 0.14	20.34 ± 0.98
M, 3.5 L/min	28.45 ± 0.80	21.20 ± 0.53	7.247 ± 0.39	77.56 ± 2.6
R, 3.5 L/min	20.83 ± 2.7	15.05 ± 2.1	5.782 ± 0.39	49.87 ± 9.1
Nw, 3.5 L/min	11.27 ± 1.3	7.297 ± 0.99	3.968 ± 0.34	18.19 ± 1.7
Mw, 3.5 L/min	24.86 ± 0.23	18.47 ± 0.44	6.389 ± 0.39	62.18 ± 4.7
Rw, 3.5 L/min	16.30 ± 1.8	11.67 ± 1.5	4.631 ± 0.33	41.77 ± 8.2
M, 5.0 L/min	52.79 ± 1.0	40.94 ± 1.1	11.85 ± 0.37	179.7 ± 17
R, 5.0 L/min	35.49 ± 3.7	26.14 ± 3.6	9.353 ± 0.21	93.79 ± 21

N = NHC, M = MAC, R = RMS, w = simulation with water rather than blood dynamic viscosity

Table 6 Average planar viscous energy dissipation rate time integrals and maximum value during respective parts of the cycle with standard deviation over the last five consecutive cycles. The velocity normal to the plane was excluded

Case	Total (erg/mL)	Diastole (erg/mL)	Systole (erg/mL)	Max (erg/s/mL)
N, 1.5 L/min	2.165 ± 0.087	1.470 ± 0.058	0.6956 ± 0.035	4.875 ± 0.15
M, 1.5 L/min	7.484 ± 0.64	6.035 ± 0.55	1.448 ± 0.094	19.14 ± 1.3
R, 1.5 L/min	6.512 ± 0.78	5.123 ± 0.74	1.388 ± 0.043	17.09 ± 2.6
N, 3.0 L/min	6.398 ± 0.54	4.431 ± 0.36	1.967 ± 0.18	11.93 ± 0.91
M, 3.0 L/min	22.87 ± 1.4	18.97 ± 1.1	3.906 ± 0.27	67.14 ± 0.79
R, 3.0 L/min	18.76 ± 1.4	15.20 ± 1.4	3.559 ± 0.089	62.32 ± 4.2
N, 3.5 L/min	8.115 ± 0.46	5.502 ± 0.39	2.614 ± 0.090	14.56 ± 1.0
M, 3.5 L/min	29.29 ± 1.5	24.43 ± 1.3	4.867 ± 0.22	89.78 ± 4.8
R, 3.5 L/min	23.36 ± 2.3	19.09 ± 2.4	4.272 ± 0.11	76.13 ± 13
Nw, 3.5 L/min	11.62 ± 0.69	7.941 ± 0.55	3.679 ± 0.089	19.21 ± 0.95
Mw, 3.5 L/min	30.99 ± 1.5	25.10 ± 1.3	5.894 ± 0.26	82.92 ± 7.5
Rw, 3.5 L/min	22.77 ± 2.3	18.14 ± 2.1	4.630 ± 0.25	76.59 ± 14
M, 5.0 L/min	52.36 ± 2.5	44.27 ± 2.3	8.092 ± 0.45	193.6 ± 15
R, 5.0 L/min	36.41 ± 3.4	29.71 ± 3.6	6.707 ± 0.20	112.1 ± 13

N = NHC, M = MAC, R = RMS, w = simulation with water rather than blood dynamic viscosity

Flow Field and Vortex Visualization

The increased energetics in the diseased cases suggests a disruption of the MV vortex, so we visualized the planar vorticity of each valve during early diastole for the 3.5 L/min CO for both water and blood analog (Fig. 6, Fig. S2, Fig. S3) and the 5.0 L/min cases (Fig. S4), using the same plane as for the planar energetics analysis. In Fig. 6 we superimposed the velocity vectors over the vorticity, and the NHC shows the MV vortex with the curl of the velocity vectors around the mitral leaflets. The MAC case velocity vectors show a disruption of the MV vortex as the vector field is directed toward the apex with the anterior bias indicated in Table 1. Similarly, the MV vortex is disrupted in the RMS valve with the mitral jet being directed at the inferolateral wall.

We further characterized the vortex disruption by generating streamlines of the velocity field at the same time point (Fig. S3). The streamlines in the NHC show the trajectory curls around the MV leaflets. In contrast, while there is some deflection of the streamlines at the leaflet tips for the MS cases, the characteristic curl of the streamline around the leaflets is notably absent.

In Fig. 6, when comparing the vorticity fields between the water and blood analog cases, there are qualitatively more vortical structures with higher vorticity magnitude, especially toward the LV apex. This supports the observation that there is more viscous dissipation during systole with water as compared to blood analog as these snapshots are taken

Table 7 Average three-dimensional kinetic energy time integrals and max value during respective parts of the cycle with standard deviation over the last five consecutive cycles. All velocity components were included in the analysis

Case	Total (erg˙s/mL)	Diastole (erg˙s/mL)	Systole (erg˙s/mL)	Max (erg/mL)
N, 1.5 L/min	0.7244 ± 0.12	0.4314 ± 0.082	0.2930 ± 0.035	1.223 ± 0.12
M, 1.5 L/min	1.764 ± 0.31	1.144 ± 0.22	0.6200 ± 0.098	2.575 ± 0.40
R, 1.5 L/min	0.7137 ± 0.15	0.4235 ± 0.10	0.2902 ± 0.046	1.177 ± 0.16
N, 3.0 L/min	2.488 ± 0.34	1.510 ± 0.24	0.9783 ± 0.10	4.200 ± 0.36
M, 3.0 L/min	6.340 ± 0.62	4.314 ± 0.47	2.026 ± 0.15	11.52 ± 0.88
R, 3.0 L/min	3.011 ± 0.53	1.883 ± 0.38	1.128 ± 0.15	4.867 ± 0.77
N, 3.5 L/min	3.245 ± 0.30	1.982 ± 0.22	1.263 ± 0.079	5.458 ± 0.29
M, 3.5 L/min	8.534 ± 0.59	5.890 ± 0.46	2.645 ± 0.14	16.68 ± 0.98
R, 3.5 L/min	4.098 ± 0.72	2.575 ± 0.52	1.522 ± 0.20	6.774 ± 1.2
Nw, 3.5 L/min	3.027 ± 0.46	1.878 ± 0.32	1.149 ± 0.14	4.833 ± 0.48
Mw, 3.5 L/min	6.835 ± 0.69	4.679 ± 0.49	2.156 ± 0.20	13.03 ± 0.93
Rw, 3.5 L/min	3.173 ± 0.60	1.981 ± 0.43	1.192 ± 0.18	5.319 ± 0.93
M, 5.0 L/min	16.08 ± 0.39	11.30 ± 0.36	4.781 ± 0.10	35.56 ± 1.1
R, 5.0 L/min	7.808 ± 1.3	4.903 ± 0.99	2.905 ± 0.33	13.14 ± 2.2

N = NHC, M = MAC, R = RMS, w = simulation with water rather than blood dynamic viscosity

Table 8 Average three-dimensional viscous energy dissipation rate time integrals and max value during respective parts of the cycle with standard deviation over the last five consecutive cycles. All velocity components were included in the analysis

Case	Total (erg/mL)	Diastole (erg/mL)	Systole (erg/mL)	Max (erg/s/mL)
N, 1.5 L/min	0.7400 ± 0.10	0.4958 ± 0.074	0.2442 ± 0.027	1.310 ± 0.18
M, 1.5 L/min	2.078 ± 0.20	1.579 ± 0.16	0.4989 ± 0.046	4.594 ± 0.31
R, 1.5 L/min	0.9649 ± 0.14	0.7182 ± 0.12	0.2467 ± 0.023	2.154 ± 0.33
N, 3.0 L/min	2.840 ± 0.27	1.942 ± 0.19	0.8979 ± 0.084	4.800 ± 0.44
M, 3.0 L/min	8.200 ± 0.62	6.375 ± 0.45	1.825 ± 0.17	20.18 ± 0.26
R, 3.0 L/min	4.050 ± 0.56	3.051 ± 0.45	0.9986 ± 0.11	10.94 ± 1.2
N, 3.5 L/min	3.835 ± 0.28	2.605 ± 0.23	1.231 ± 0.057	6.419 ± 0.65
M, 3.5 L/min	11.01 ± 0.68	8.721 ± 0.55	2.292 ± 0.13	29.79 ± 1.9
R, 3.5 L/min	5.341 ± 0.69	4.027 ± 0.59	1.314 ± 0.10	14.40 ± 2.3
Nw, 3.5 L/min	5.509 ± 0.48	3.681 ± 0.34	1.829 ± 0.14	7.945 ± 0.72
Mw, 3.5 L/min	12.42 ± 0.76	9.496 ± 0.54	2.927 ± 0.23	30.02 ± 1.8
Rw, 3.5 L/min	5.821 ± 0.85	4.264 ± 0.67	1.557 ± 0.18	14.36 ± 2.5
M, 5.0 L/min	21.26 ± 0.94	16.92 ± 0.89	4.343 ± 0.14	68.02 ± 3.4
R, 5.0 L/min	9.824 ± 1.3	7.268 ± 1.2	2.556 ± 0.19	25.20 ± 3.9

N = NHC, M = MAC, R = RMS, w = simulation with water rather than blood dynamic viscosity

during early diastole. Beyond the increased persistent vorticity, the flow fields do not qualitatively differ significantly between blood analog and water.

Flow Analysis through Advecting Particles

We conducted a particle tracking experiment during the simulations to query whether the valve geometries impacted particle retention times and ventricular washout and admixture. For this, we released 2000 massless particles upstream of the mitral valve just before the onset of the second diastolic phase (at 1.4 s out of a 7.0 s simulation) to advect with the fluid. The particle positions were tracked with respect to the mitral and AV annuli to compute the distance traveled as well as the entry and exit times into and out of the ventricle, respectively.

We first conducted a qualitative analysis of the particle traces by tracking the particle displacements from beat-to-beat for three cycles after the particle release time for the 3.5 L/min CO simulations with blood analog (Fig. 7) and water (Fig. S5) and for the 5.0 L/min simulation (Fig. S6). For the NHC with blood analog and water at 3.5 L/min, the particles exit the MV and are deposited around the mitral leaflets, leaving the particles near the LV outflow tract (LVOT) midventricle. By late systole in the third cycle after release, 244 particles have been ejected from the LV in the blood analog simulation and 151 particles have been ejected for the water simulation. The particles in the MAC case are directed toward the apex and then disperse in the lower half of the LV

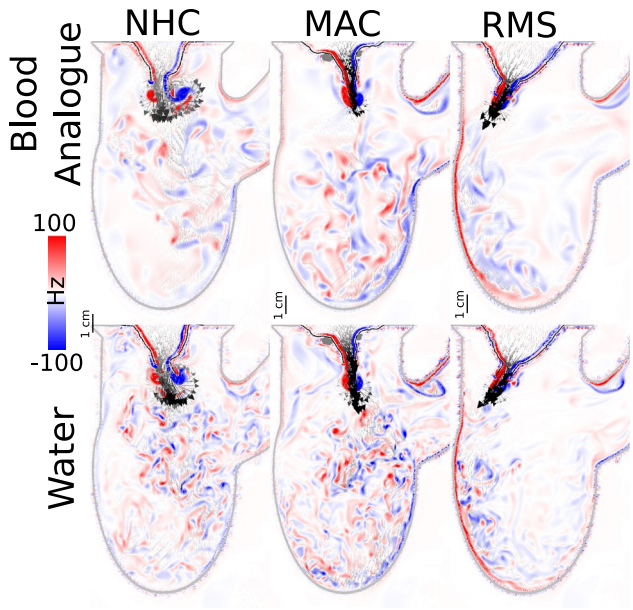


Fig. 6 Snapshots of the planar vorticity with the velocity vectors during early diastole for the blood analog and water simulations at 3.5 L/min. Just the vorticity and vorticity with streamlines are included in Fig. S2 and Fig. S3, respectively

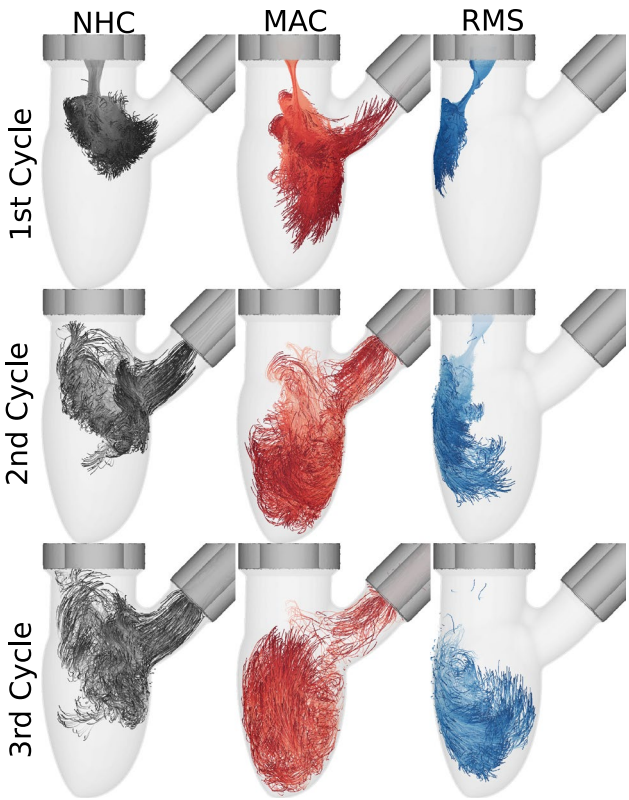


Fig. 7 Particle traces one, two, and three cycles after particle release for the 3.5 L/min simulations with blood analog. The particle tails correspond to the path each particle has taken over the previous cycle. The time point corresponds to the end of systole (see 1.4 seconds in Fig. S1 for the corresponding pump phase)

below the LVOT, and 220 particles have been ejected with blood analog and 162 with water by the third cycle at 3.5 L/min. The particle traces from the RMS valve are initially directed at the inferolateral wall, and then the particles travel along the LV wall toward the LV apex opposite the LVOT—no particles have been ejected with water or blood analog by the third cycle at 3.5 L/min in the RMS case. These particle traces reflect and reinforce the initial flow visualizations as seen in Fig. 6.

We computed the displacements and retention times of the particles to make quantitative comparisons of the qualitative results (Fig. 8, Tables 9 and 10). A large immediate difference between the valves is the number of ejected particles. Table 9 contains the summary statistics for the ejected particles for each valve. In the 1.5 L/min simulations, only the NHC valve had any particles ejected with 77. The particle ejection count was much larger at 3.5 L/min with blood analog, and all valves resulted in ejected particles with 708, 396, and 107 ejected particles for the NHC, MAC, and RMS valves, respectively. The number of ejected particles was depressed for the simulations using water as the test fluid at 3.5 L/min with 643, 284, and 8 ejected particles for the NHC, MAC, and RMS valves, respectively.

For the ejected particles, the average displacement (Fig. 8a; Table 9), truncated when the particle exited the LV, was highest for the RMS case compared to the other valves at 3.5 L/min and 5.0 L/min ($p < 1e{-}10$) and not statistically different between the NHC and MAC cases at 3.5 L/min ($p > 0.2$). The average displacement decreased for the MAC-associated MS and NHC cases from the blood analog to water simulations ($p < 1e{-}4$). With blood analog, the mean ejected-particle distance traveled increased from 3.5 to 5.0 L/min in both diseased cases. The ejected particle retention time was largest for the RMS case for the 3.5 L/min and 5.0 L/min simulations ($p < 1e{-}10$), while the MAC case had the smallest retention times ($p < 1e{-}10$) with the largest variance. The retention time only changed with water for the RMS case, where the retention time increased ($p < 0.01$). From 3.5 L/min to 5.0 L/min, the retention times decreased in the RMS case ($p < 1e{-}7$), but there was no change in the MAC case.

As most of the particles were not ejected regardless of valve type, we calculated the total displacements and the retention times (calculated as the difference between the time of entry into the ventricle and the simulation end time). Table 10 contains the summary statistics for these data. For each CO, the retained MAC particles undergo the largest total displacements ($p < 1e{-}10$), whereas the retained particles in the NHC undergo the least total displacement

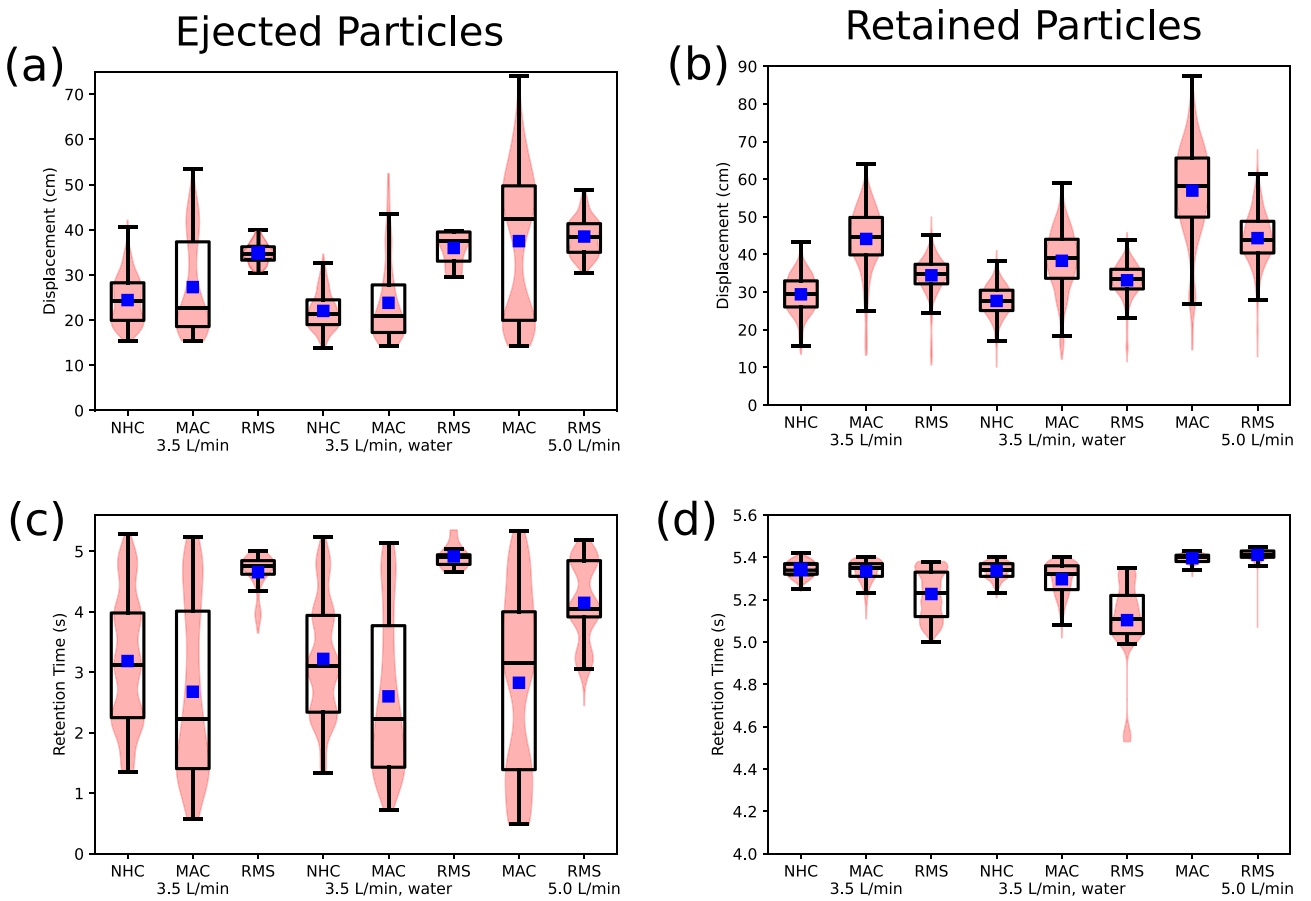


Fig. 8 Distributions of displacements (**a-b**) and retention times (**c, d**) for particles that circulated through the left ventricle and were ejected (**a, c**) and particles that entered the ventricle but were not ejected (**b, d**). The retention times for the retained particles were computed using the time the particle entered the ventricle to the end of the simulation at 7 s. The displacement values for the ejected particles consider only the distance traveled while within the ventricle

($p < 1e{-}10$), as seen in Fig. 8(b). Displacements and retention times are consistently larger in the blood analog cases compared to water at 3.5 L/min across all valves ($p < 1e{-}10$). At 1.5, 3.0, and 3.5 L/min, retention times are largest in the NHC ($p < 1e{-}10$) and smallest for RMS ($p < 1e{-}10$). Retention times consistently increase with CO from 3.5 to 5.0 L/min.

Discussion

In this study, we compared MAC-associated MS to RMS using patient-specific MV geometries within a high-fidelity FSI framework, with an NHC valve as a reference across various COs. The experimental design was based on a previously published *in vitro* configuration [5], and we extended prior planar PIV analyses to fully three-dimensional flow fields. This approach enabled quantification of transmitral pressure gradients, velocities, kinetic energy, and viscous energy dissipation, while also providing direct assessment of vortex formation and intraventricular transport. Planar energetics were computed to enable comparison with PIV methods, and particle advection was used to interrogate ventricular washout and residence times.

General Trends

Transmitral pressure gradients behaved as expected from other work [5, 7], with both RMS and MAC cases exhibiting elevated mean and peak gradients relative to the NHC valve. The mean gradient was not significantly different between the two diseased cases at the higher, more physiologic flow rates of 3.5 L/min and 5.0 L/min, despite the EOA of the RMS case being consistently smaller than the MAC case. This reflects previous *in vitro* results as the mean gradient is larger in the MAC case when scaled by the EOA ($p < 5e{-}3$) [13]. At 3.5 L/min, peak velocity was higher in RMS than MAC for both fluid properties, whereas MAC had the higher peak velocity at 5.0 L/min. Hence, when interpreted in the

context of orifice area scaling, the effective hemodynamic burden is greater in MAC consistent with other work [5], as a significantly larger orifice area (> 40% for 3.5 L/min and 5.0 L/min) should translate to reduced velocities and reduced pressure gradients given similar flow conditions.

Energetic analysis supports a greater hemodynamic burden in the MAC case as compared to RMS, reflective of previous *in vitro* work [5]. Pump stroke work was highest in the MAC case across all COs, suggesting that greater mechanical energy input is required to sustain equivalent flow conditions. This trend was supported by both planar and three-dimensional kinetic energy and viscous dissipation metrics. While planar estimates suggested comparable peak dissipation between RMS and MAC at lower COs (3.0 L/min), three-dimensional analysis revealed significantly elevated viscous dissipation in MAC. Time-integrated dissipation further amplified this distinction, demonstrating that MAC imposes a larger cumulative energetic penalty over the cardiac cycle.

The large proportional difference in the energetics between the three-dimensional and planar energy analysis is most attributable to the large difference in the out-of-plane (defined by the plane that bisects the MV and AV) velocity between MAC and the NHC and RMS cases (Fig. S8). For example, there is a 35% reduction in maximum planar kinetic energy between MAC and RMS at 3.5 L/min with blood analog, while there is a 59% reduction in the maximum three-dimensional kinetic energy. This extends to the dissipation rates as well, with a 20% reduction between MAC and RMS in the total dissipation over the cycle with planar measurements and a 51% reduction when using three-dimensional metrics for the same 3.5 L/min simulations with blood analog. As RMS and the NHC have comparable out-of-plane velocity values, the planar metrics overestimate the differences in the maximum kinetic energies (59% planar to 19% three-dimensional difference from RMS to the NHC, 3.5 L/min blood analog) and the total dissipation (65% planar to 28% three-dimensional reduction from RMS to the NHC, 3.5 L/min blood analog). These differences would not be available through planar analysis.

Notably, these energetic differences were not confined to diastole. Elevated energy levels persisted into systole in both states of disease, indicating that altered inflow conditions propagate to affect global ventricular flow dynamics. This behavior is consistent with disruption of the mitral vortex, which normally promotes efficient momentum redistribution and minimizes dissipation throughout the cycle [57]. The greater energetic burden observed in MAC suggests a more severe impairment of this flow-mediated efficiency mechanism compared to RMS.

Flow visualization supports this interpretation. The NHC valve produced a coherent diastolic vortex, whereas both diseased valves generated jet-dominated inflow with absent or severely attenuated vortex structures (Fig. 6). The MAC-associated MS jet was directed toward the ventricular apex, while the RMS jet impinged on the inferolateral wall, consistent with geometric bias angles. These distinct jet orientations reflect underlying structural differences and may lead to spatially heterogeneous wall loading, with potential implications for ventricular remodeling.

Particle advection analysis further differentiated transport dynamics between cases. In the NHC configuration, vortex formation promoted efficient washout, shorter residence times, and preferential transport toward the outflow tract,

Table 9 Summary statistics for particles ejected from the release time (1.4 s) to the simulation end time (7.0 s) for each valve type. Distance traveled was only computed until the particle left the ventricle. Reported values are mean and standard deviation

Case	Particles ejected	Distance traveled (cm)	Retention time (s)
N, 1.5 L/min	77 (3.85%)	18.60 ± 0.78	3.801 ± 0.55
M, 1.5 L/min	0 (0%)	N/A	N/A
R, 1.5 L/min	0 (0%)	N/A	N/A
N, 3.0 L/min	593 (29.65%)	23.02 ± 4.0	3.440 ± 0.93
M, 3.0 L/min	186 (9.3%)	33.95 ± 3.7	4.333 ± 0.48
R, 3.0 L/min	7 (0.35%)	33.12 ± 1.7	4.357 ± 0.28
N, 3.5 L/min	708 (35.4%)	24.44 ± 4.2	3.186 ± 1.1
M, 3.5 L/min	396 (19.8%)	27.31 ± 10	2.678 ± 1.4
R, 3.5 L/min	107 (5.35%)	34.82 ± 2.2	4.653 ± 0.31
Nw, 3.5 L/min	643 (32.15%)	22.04 ± 4.1	3.221 ± 0.94
Mw, 3.5 L/min	284 (14.2%)	23.83 ± 8.4	2.602 ± 1.3
Rw, 3.5 L/min	8 (0.4%)	35.98 ± 3.9	4.914 ± 0.31
M, 5.0 L/min	501 (25.05%)	37.49 ± 16	2.826 ± 1.5
R, 5.0 L/min	235 (11.75%)	38.50 ± 4.1	4.148 ± 0.64

N = NHC, M = MAC, R = RMS, w = simulation with water rather than blood dynamic viscosity

Table 10 Summary statistics for particles that entered the ventricle from the release time (1.4 s) to the simulation end time (7.0 s) for each valve type. Retention time in this context was computed from each particle's respective entry time into the ventricle to the end of the simulation (7.0 s). Reported values are mean and standard deviation

Case	Particles retained	Distance traveled (cm)	Retention time (s)
N, 1.5 L/min	1923 (96.15%)	18.74 ± 2.2	4.625 ± 0.24
M, 1.5 L/min	2000 (100%)	24.63 ± 3.4	4.611 ± 0.18
R, 1.5 L/min	2000 (100%)	21.47 ± 2.4	3.836 ± 0.32
N, 3.0 L/min	1407 (70.35%)	26.40 ± 4.4	5.312 ± 0.051
M, 3.0 L/min	1814 (90.7%)	37.24 ± 5.9	5.252 ± 0.093
R, 3.0 L/min	1993 (99.65%)	32.05 ± 4.3	5.005 ± 0.24
N, 3.5 L/min	1292 (64.6%)	29.41 ± 4.9	5.344 ± 0.036
M, 3.5 L/min	1604 (80.2%)	44.12 ± 8.3	5.334 ± 0.053
R, 3.5 L/min	1893 (94.65%)	34.46 ± 5.1	5.227 ± 0.11
Nw, 3.5 L/min	1357 (67.85%)	27.65 ± 4.1	5.337 ± 0.037
Mw, 3.5 L/min	1716 (85.8%)	38.31 ± 8.2	5.297 ± 0.075
Rw, 3.5 L/min	1992 (99.6%)	33.14 ± 4.6	5.103 ± 0.19
M, 5.0 L/min	1499 (74.95%)	56.96 ± 12	5.396 ± 0.018
R, 5.0 L/min	1765 (88.25%)	44.34 ± 7.0	5.411 ± 0.024

N = NHC, M = MAC, R = RMS, w = simulation with water rather than blood dynamic viscosity

resulting in higher particle ejection rates. In contrast, both RMS and MAC exhibited reduced ejection efficiency and longer intraventricular trajectories. The MAC case showed the largest displacements among retained particles, consistent with inefficient recirculation and increased path length, whereas the RMS case exhibited the longest retention times among ejected particles, indicating delayed inflow progression and reduced mixing efficiency. These results suggest that MAC and RMS impair transport through distinct mechanisms; MAC primarily through increased energetic loss and flow dispersion, and RMS through geometric restriction and delayed filling.

Clinical Implications

Breathlessness and effort intolerance are the hallmarks of valvular disease. In RMS symptoms typically appear when the geometric orifice area falls below 1.5 cm^2 at which point intervention is warranted [3]. MAC-associated MS is more complex, and specific guidelines for intervention are limited [3]. Affected patients are typically older than those with RMS and have more comorbidities [57]. It is often unclear whether patient symptoms and effort intolerance are due to the valve abnormality or the abnormal atrial and ventricular compliance that typically accompany MAC-associated MS [58]. Importantly, intervention is more difficult and carries greater risk in this disease state than in RMS [59].

It is therefore imperative to understand the effects of MAC-associated MS on flow dynamics across the MV. If the physiologic derangements are primarily due to abnormal chamber compliance, then valve replacement may incur greater risk than benefit. Conversely, if geometric distortion of the valve apparatus is the primary driver, then valve intervention might be justified. The present findings suggest that the valve geometry itself plays an important role. However, the distribution and severity of MAC, and its effects on valve geometry, are highly variable, and the present study includes only a single representative case. Future studies involving larger patient cohorts are needed to determine which specific geometric characteristics of this increasingly common disease have the greatest influence on intraventricular flow and myocardial energetics.

Blood Analog Versus Water

From the blood analog and water simulations at 3.5 L/min, we were able to highlight some specific differences that may arise when using water as the carrying liquid. Water consistently reduced the pump stroke work ($p < 5e{-}3$), reduced the maximum pressure gradient ($p < 0.01$), and increased the Reynolds number ($p < 5e{-}3$) across all valves. Additionally, for the diseased valves, there were smaller max velocities ($p < 0.01$) and reduced mean transmitral gradients ($p < 0.03$). These effects may be due to the reduced boundary layer size from a reduction in dynamic viscosity. The effect would potentially be more pronounced for the smaller orifice openings as the boundary layer would be proportionally larger in the diseased cases, hence the insignificant changes to the maximum velocity and the mean pressure gradient in the NHC.

At 3.5 L/min, mean pump stroke work and cycle-integrated kinetic energy are higher with blood analog, whereas cycle-integrated three-dimensional viscous energy dissipation is higher with water. Systolic time-integrated viscous energy dissipation is also higher with water. This could be explained by the observation that most of the vorticity within

the ventricle is due to the mitral valve vortex during diastole [57] and vortex decay is accelerated by increased viscosity. Hence, vortical decay is slower for the water simulations and the dissipation rate remains higher during systole, as was quantified. The larger vorticity in water compared to blood analog during early diastole can be seen in Fig. 6.

In Vitro Comparison

While the geometries and the pump flow rates were derived from the same sources as the *in vitro* work done in Hashemi *et al*. [5], there are differences in the results that may be due to missing implementation details. The most evident difference is the larger velocities seen in the MAC case as compared to RMS in the *in vitro* work that is not observed *in silico* until the 5.0 L/min simulations. Further, the EOAs *in vitro* are smaller for all valves than what was computed from the *in silico* data, and the peak NHC velocity is also reduced *in silico* (~30% smaller). This last discrepancy may be because of the difference in the NHC orifice geometric area as none is reported *in vitro* for a reference, and we had to interpret how deep to make the commissures from available images. Further, as the pressure data from the *in vitro* work was not available, we chose to make the pressure boundary conditions upstream of the MV to be 10 mmHg to match atrial physiology, and for the pressure boundary conditions downstream of the AV to sit around 10 mmHg to prevent MV inversion. The choice of pressure boundary conditions could ultimately affect the differences we see in the velocity values and the velocity relation between the diseased cases.

The qualitative trends with the vortex disruption in the diseased cases (**Fig. S7**) were consistent between the *in silico* and *in vitro* work; however, and additionally, we demonstrated the same comparative quantitative energetic relations between the diseased cases seen *in vitro* as we observed larger kinetic energies and viscous energy dissipation rates for the MAC case as compared to RMS with both planar and three-dimensional analyses. As such, we believe this work provides a proof-of-concept for replicating this *in vitro* system *in silico* and extending the results to alternate loading conditions, different fluid properties, and three-dimensional analyses, while highlighting the need for comprehensive flow rate and pressure data to accurately define loading conditions for more direct comparison and future validation work.

Limitations

This study has several limitations that should be considered when interpreting the results. The left ventricular geometry was larger than physiological size and resulted in a reduced ejection fraction (9.4% at 5.0 L/min), which may influence flow structure, vortex formation, and particle transport.

Only a single representative valve geometry was examined for each disease etiology, limiting the ability to assess inter-patient variability. Material properties were simplified, with isotropic silicone representations for the leaflets and a fully rigid approximation of the calcification for the MAC case, whereas native tissues exhibit more complex, anisotropic, and partially compliant behavior. In addition, the absence of the subvalvular apparatus (chordae tendineae and papillary muscles) reduces physiological fidelity and may affect flow dynamics. The lack of a subvalvular complex also reduced the loading conditions of the system as the NHC model fully inverted with CO greater than 3.5 L/min from the increased LV pressure.

Finally, while the simulations provide detailed three-dimensional flow information, direct validation with volumetric experimental or *in vivo* data was not performed. Comparisons were made to the observations of past *in vitro* work [5, 7, 13], but we were unable to fully recreate the experimental design of Hashemi *et al*. [5], on which this work is based, as pressure measurements were unavailable. Potential differences in the pressure loading conditions may have contributed to the discrepancies noted between this present study and the *in vitro* work of Hashemi *et al*. [5]. Future studies incorporating larger cohorts, more physiological material models, subvalvular structures, and complementary validation data would strengthen these findings.

Conclusions

In conclusion, we have presented a proof-of-concept three-dimensional FSI study suggesting that MAC-associated MS may impose a greater energetic burden on ventricular flow than rheumatic disease, despite its larger orifice area and lack of consistently higher mean transmitral pressure gradients or peak transmitral velocities. Importantly, three-dimensional analysis exposed differences that are not captured by planar measurements, emphasizing the need for volumetric flow assessment in studies of cardiac energetics. Both diseased valve types disrupted mitral vortex formation, but through distinct flow mechanisms that differentially affect energy dissipation and transport efficiency. These findings support the possible existence of etiology-specific hemodynamic signatures and provide a mechanistic basis for potentially improved characterization of mitral stenosis beyond

standard clinical metrics. However, further study with an extended valve cohort is needed.

Supplementary Information The online version contains supplementary material available at https://doi.org/10.1007/s10439-026-04364-7.

Acknowledgements Computations were performed using facilities provided by University of North Carolina at Chapel Hill through the Research Computing division of UNC Information Technology Services. This manuscript is the result of funding in whole or in part by the National Institutes of Health (NIH). It is subject to the NIH Public Access Policy. Through acceptance of this federal funding, NIH has been given a right to make this manuscript publicly available in PubMed Central upon the Official Date of Publication, as defined by NIH.

Author Contributions Marshall Davey: Conceptualization, data curation, formal analysis, investigation, methodology, software, visualization, writing–original draft, writing–review and editing; Mohammad Saber Hashemi: Conceptualization, data curation, methodology, writing–review and editing; Gregg S Pressman: Conceptualization, data curation, methodology, writing–review and editing; Arash Kheradvar: Conceptualization, methodology, supervision, writing–review and editing; Boyce E Griffith: Conceptualization, methodology, software, supervision, writing–review and editing.

Funding National Heart, Lung, and Blood Institute, HL153724, Arash Kheradvar, HL157631, Boyce E. Griffith, HL162687, Arash Kheradvar, HL182166, Boyce E. Griffith, HL173809, Arash Kheradvar, National Science Foundation, CBET 2109959, Arash Kheradvar, OAC 1931516, Boyce E. Griffith.

Data Availability The *in silico* data acquired and analyzed during this study as well as the computational model are available from the corresponding author upon reasonable request.

Open Access This article is licensed under a Creative Commons Attribution 4.0 International License, which permits use, sharing, adaptation, distribution and reproduction in any medium or format, as long as you give appropriate credit to the original author(s) and the source, provide a link to the Creative Commons licence, and indicate if changes were made. The images or other third party material in this article are included in the article's Creative Commons licence, unless indicated otherwise in a credit line to the material. If material is not included in the article's Creative Commons licence and your intended use is not permitted by statutory regulation or exceeds the permitted use, you will need to obtain permission directly from the copyright holder. To view a copy of this licence, visit http://creativecommons.org/licenses/by/4.0/.

References

1. Iung, B., and A. Vahanian. Epidemiology of acquired valvular heart disease. *Can. J. Cardiol.* 30(9):962–970, 2014.
2. Kato, N., M. Guerrero, R. Padang, J. M. Amadio, M. F. Eleid, C. G. Scott, A. T. Lee, S. V. Pislaru, V. T. Nkomo, and P. A. Pellikka. Prevalence and Natural History of Mitral Annulus Calcification and Related Valve Dysfunction. *Mayo Clin. Proc.* 97(6):1094–1107, 2022.
3. Otto, C. M., R. A. Nishimura, R. O. Bonow, B. A. Carabello, J. P. Erwin 3rd., F. Gentile, H. Jneid, E. V. Krieger, M. Mack, C. McLeod, P. T. O'Gara, V. H. Rigolin, T. M. Sundt 3rd., A. Thompson, and C. Toly. 2020 ACC/AHA Guideline for the Management of Patients With Valvular Heart Disease: A Report of the American College of Cardiology/American Heart Association Joint Committee on Clinical Practice Guidelines. *Circulation*. 143(5):e72–e227, 2021.
4. Liu, Z., R. Liu, J. Liang, M. Wang, M. Wang, H. Zhang, and W. Jiang. Chronic mitral valve fibrosis in rheumatic heart disease: from immune trigger to inflammatory and mechanical progression. *J. Am. Heart Assoc.* 14(22):e045169, 2025.
5. Hashemi, M. S., P. Abdelmaseeh, A. Nehvi, G. S. Pressman, and A. Kheradvar. Two Faces of Mitral Stenosis: Uncovering Structural and Hemodynamic Signatures of Rheumatic and Mitral Annular Calcification-Induced Disease. *J. Am. Heart Assoc.* 15(3):e045018, 2026.
6. Ambhore, A., J. N. Ngiam, N. W. S. Chew, T. Pramotedham, J. P. Y. Loh, G. S. Kang, and K. K. Poh. Optimal vortex formation time index in mitral valve stenosis. *Int. J. Cardiovasc. Imaging*. 37(5):1595–1600, 2021.
7. Wiener, P. C., A. Darwish, E. Friend, L. Kadem, and G. S. Pressman. Energy loss associated with in-vitro modeling of mitral annular calcification. *PLoS One*. 16(2):e0246701, 2021.
8. Elbaz, M. S. M., E. E. Calkoen, J. J. M. Westenberg, B. P. F. Lelieveldt, A. A. W. Roest, and R. J. van der Geest. Vortex flow during early and late left ventricular filling in normal subjects: quantitative characterization using retrospectively-gated 4D flow cardiovascular magnetic resonance and three-dimensional vortex core analysis. *J. Cardiovasc. Magn. Reson.* 16(1):78, 2014.
9. Falahatpisheh, A., N. M. Pahlevan, and A. Kheradvar. Effect of the mitral valve's anterior leaflet on axisymmetry of transmitral vortex ring. *Ann. Biomed. Eng.* 43(10):2349–2360, 2015.
10. Gharib, M., E. Rambod, A. Kheradvar, D. J. Sahn, and J. O. Dabiri. Optimal vortex formation as an index of cardiac health. *Proc. Natl. Acad. Sci. U. S. A.* 103(16):6305–6308, 2006.
11. Kheradvar, A., and M. Gharib. On mitral valve dynamics and its connection to early diastolic flow. *Ann. Biomed. Eng.* 37(1):1–13, 2009.
12. Kheradvar, A., C. Rickers, D. Morisawa, M. Kim, G. R. Hong, and G. Pedrizzetti. Diagnostic and prognostic significance of cardiovascular vortex formation. *J. Cardiol.* 74(5):403–411, 2019.
13. Gilon, D., E. G. Cape, M. D. Handschumacher, L. Jiang, C. Sears, J. Solheim, E. Morris, J. T. Strobel, S. M. Miller-Jones, A. E. Weyman, and R. A. Levine. Insights from three-dimensional echocardiographic laser stereolithography. Effect of leaflet funnel geometry on the coefficient of orifice contraction, pressure loss, and the Gorlin formula in mitral stenosis. *Circulation*. 94(3):452–459, 1996.
14. Herrmann, T. A., A. W. Siefert, G. S. Pressman, H. R. Gollin, S. A. Touchton Jr., N. Saikrishnan, and A. P. Yoganathan. In vitro comparison of Doppler and catheter-measured pressure gradients in 3D models of mitral valve calcification. *J. Biomech. Eng.* 135(9):094502, 2013.
15. Park, M. H., P. K. Pandya, Y. Zhu, D. M. Mullis, H. Wang, A. M. Imbrie-Moore, R. Wilkerson, M. Marin-Cuartas, and Y. J. Woo. A Novel Rheumatic Mitral Valve Disease Model with Ex Vivo Hemodynamic and Biomechanical Validation. *Cardiovasc. Eng. Technol.* 14(1):129–140, 2023.
16. Zhu, Y., S. Yajima, R. J. Wilkerson, M. H. Park, J. Y. Kim, P. K. Pandya, and Y. J. Woo. Anterior Pericardial Patch Augmentation Repair and Neochord Implantation for Rheumatic Mitral Valves. *Ann. Thorac. Surg. Short Rep.* 1(2):302–306, 2023.
17. Kheradvar, A., J. Kasalko, D. Johnson, and M. Gharib. An in vitro study of changing profile heights in mitral bioprostheses and their influence on flow. *ASAIO J.* 52(1):34–38, 2006.
18. Scarsoglio, S., A. Saglietto, F. Gaita, L. Ridolfi, and M. Anselmino. Computational fluid dynamics modelling of left valvular heart diseases during atrial fibrillation. *PeerJ*. 4:e2240, 2016.
19. van den Acker, G. P. H., S. Dhont, T. van Loon, T. W. Churchill, F. Timmermans, T. Delhaas, P. B. Bertrand, and J. Lumens. Impact

of left-heart myopathy on mitral valve stenosis assessment and interventional outcomes: an in-silico trial. *Eur. Heart J. Digit. Health.* 7(1):ztaf097, 2026.
20. Lau, K. D., V. Diaz, P. Scambler, and G. Burriesci. Mitral valve dynamics in structural and fluid-structure interaction models. *Med. Eng. Phys.* 32(9):1057–1064, 2010.
21. Caballero, A., W. Mao, R. McKay, C. Primiano, S. Hashim, and W. Sun. New insights into mitral heart valve prolapse after chordae rupture through fluid-structure interaction computational modeling. *Sci. Rep.* 8(1):17306, 2018.
22. Caballero, A., W. Mao, R. McKay, and W. Sun. Transapical mitral valve repair with neochordae implantation: FSI analysis of neochordae number and complexity of leaflet prolapse. *Int. J. Numer. Meth. Biomed. Eng.* 36(3):e3297, 2020.
23. Mao, W., A. Caballero, R. McKay, C. Primiano, and W. Sun. Fully-coupled fluid-structure interaction simulation of the aortic and mitral valves in a realistic 3D left ventricle model. *PLoS One*. 12(9):e0184729, 2017.
24. Einstein, D. R., F. Del Pin, X. Jiao, A. P. Kuprat, J. P. Carson, K. S. Kunzelman, R. P. Cochran, J. M. Guccione, and M. B. Ratcliffe. Fluid-structure interactions of the mitral valve and left heart: comprehensive strategies, past, present and future. *Int. J. Numer. Meth. Biomed. Eng.* 26(3–4):348–380, 2010.
25. Kronborg, J., and J. Hoffman. Fluid-structure interaction simulation of mitral valve structures in a left ventricle model. *Int. J. Numer. Methods Eng.* 126(8):e70031, 2025.
26. Nordsletten, D., M. McCormick, P. J. Kilner, P. Hunter, D. Kay, and N. P. Smith. Fluid-solid coupling for the investigation of diastolic and systolic human left ventricular function. *Int. J. Numer. Meth. Biomed. Eng.* 27(7):1017–1039, 2011.
27. Sugiura, S., T. Washio, A. Hatano, J. Okada, H. Watanabe, and T. Hisada. Multi-scale simulations of cardiac electrophysiology and mechanics using the University of Tokyo heart simulator. *Prog. Biophys. Mol. Biol.* 110(2–3):380–389, 2012.
28. Cai, L., T. Zhao, Y. Wang, X. Luo, and H. Gao. Fluid-structure interaction simulation of pathological mitral valve dynamics in a coupled mitral valve-left ventricle model. *Intell. Med.* 3(2):104–114, 2023.
29. Chen, W. W., H. Gao, X. Y. Luo, and N. A. Hill. Study of cardiovascular function using a coupled left ventricle and systemic circulation model. *J. Biomech.* 49(12):2445–2454, 2016.
30. Gao, H., H. Wang, C. Berry, X. Luo, and B. E. Griffith. Quasi-static image-based immersed boundary-finite element model of left ventricle under diastolic loading. *Int. J. Numer. Meth. Biomed. Eng.* 30(11):1199–1222, 2014.
31. Gao, H., L. Feng, N. Qi, C. Berry, B. E. Griffith, and X. Luo. A coupled mitral valve-left ventricle model with fluid-structure interaction. *Med. Eng. Phys.* 47:128–136, 2017.
32. Lemmon, J. D., and A. P. Yoganathan. Three-dimensional computational model of left heart diastolic function with fluid-structure interaction. *J. Biomech. Eng.* 122(2):109–117, 2000.
33. Falahatpisheh, A., and A. Kheradvar. High-speed particle image velocimetry to assess cardiac fluid dynamics *in vitro*: from performance to validation. *Eur. J. Mech. B Fluids*. 35:2–8, 2012.
34. Morisawa, D., A. Falahatpisheh, E. Avenatti, S. H. Little, and A. Kheradvar. Intraventricular vortex interaction between transmitral flow and paravalvular leak. *Sci. Rep.* 8(1):15657, 2018.
35. Brindise, M. C., M. M. Busse, and P. P. Vlachos. Density and viscosity matched Newtonian and non-Newtonian blood analog solutions with PDMS refractive index. *Exp. Fluids*. 59(11):173, 2018.
36. Hu, Y., T. Schneider, B. Wang, D. Zorin, and D. Panozzo. Fast tetrahedral meshing in the wild. *ACM Trans. Graph.* 39(4):117:1–117:18, 2020.
37. Skorina, E. H., M. Luo, W. Y. Oo, W. Tao, F. Chen, S. Youssefian, N. Rahbar, and C. D. Onal. Reverse pneumatic artificial muscles (rPAMs): Modeling, integration, and control. *PLoS One*. 13(10):e0204637, 2018.
38. Lee, J. H., A. D. Rygg, E. M. Kolahdouz, S. Rossi, S. M. Retta, N. Duraiswamy, L. N. Scotten, B. A. Craven, and B. E. Griffith. Fluid-structure interaction models of bioprosthetic heart valve dynamics in an experimental pulse duplicator. *Ann. Biomed. Eng.* 48(5):1475–1490, 2020.
39. Lee, J. H., L. N. Scotten, R. Hunt, T. G. Caranasos, J. P. Vavalle, and B. E. Griffith. Bioprosthetic aortic valve diameter and thickness are directly related to leaflet fluttering: Results from a combined experimental and computational modeling study. *JTCVS Open*. 6:60–81, 2021.
40. Griffith, B. E., R. D. Hornung, D. M. McQueen, and C. S. Peskin. An adaptive, formally second order accurate version of the immersed boundary method. *J. Comput. Phys.* 223(1):10–49, 2007.
41. Griffith, B. E., R. D. Hornung, D. M. McQueen, and C. S. Peskin. Parallel and adaptive simulation of cardiac fluid dynamics. In: Advanced Computational Infrastructures for Parallel and Distributed Adaptive Applications, edited by M. Parashar and X. Li. Hoboken, NJ, USA: John Wiley and Sons, 2009, pp. 105–130.
42. Griffith, B. E., and X. Luo. Hybrid finite difference/finite element immersed boundary method. *Int. J. Numer. Meth. Biomed. Eng.* 33(12):e2888, 2017.
43. IBAMR: Immersed Boundary Adaptive Mesh Refinement Software Infrastructure. https://ibamr.github.io/. 2026.
44. Wells, D. R., B. Vadala-Roth, J. H. Lee, and B. E. Griffith. A nodal immersed finite element-finite difference method. *J. Comput. Phys.* 477:111890, 2023.
45. Hornung, R. D., and S. R. Kohn. Managing application complexity in the SAMRAI object-oriented framework. *Concurrency Computat.: Pract. Exper.* 14:347-368, 2002.
46. Balay, S., W. D. Gropp, L. C. McInnes, and B. F. Smith. Efficient management of parallelism in object oriented numerical software libraries. In: Modern Software Tools for Scientific Computing, edited by E. Arge, A. M. Bruaset, and H. P. Langtangen. Basel, CH: Birkhäuser Press, 1997, pp. 163–202.
47. Balay, S., S. Abhyankar, M. F. Adams, S. Benson, J. Brown, P. Brune, K. Buschelman, E. M. Constantinescu, L. Dalcin, A. Dener, V. Eijkhout, J. Faibussowitsch, W. D. Gropp, V. Hapla, T. Isaac, P. Jolivet, D. Karpeev, D. Kaushik, M. G. Knepley, F. Kong, S. Kruger, D. A. May, L. C. McInnes, R. T. Mills, L. Mitchell, T. Munson, J. E. Roman, K. Rupp, P. Sanan, J. Sarich, B. F. Smith, H. Suh, S. Zampini, H. Zhang, H. Zhang, and J. Zhang. PETSc/TAO users manual. ANL-21/39-Revision 3.22. Lemont, IL, USA: Argonne National Laboratory, 2024.
48. Balay, S., S. Abhyankar, M. F. Adams, S. Benson, J. Brown, P. Brune, K. Buschelman, E. M. Constantinescu, L. Dalcin, A. Dener, V. Eijkhout, J. Faibussowitsch, W. D. Gropp, V. Hapla, T. Isaac, P. Jolivet, D. Karpeev, D. Kaushik, M. G. Knepley, F. Kong, S. Kruger, D. A. May, L. C. McInnes, R. T. Mills, L. Mitchell, T. Munson, J. E. Roman, K. Rupp, P. Sanan, J. Sarich, B. F. Smith, S. Zampini, H. Zhang, H. Zhang, and J. Zhang. PETSc software web page. https://petsc.org/. 2024.
49. Arndt, D., W. Bangerth, D. Davydov, T. Heister, L. Heltai, M. Kronbichler, M. Maier, J. P. Pelteret, B. Turcksin, and D. Wells. The deal.II finite element library: design, features, and insights. *Computers & Mathematics with Applications*. 81:407–422, 2021.
50. Arndt, D., W. Bangerth, M. Bergbauer, B. Blais, M. Fehling, R. Gassmöller, T. Heister, L. Heltai, M. Kronbichler, M. Maier, P. Munch, S. Scheuerman, B. Turcksin, S. Uzunbajakau, D. Wells, and M. Wichrowski. The deal.II library, version 9.7. *J. Numer. Math.* 33(4):403–415, 2025.
51. Arndt, D., W. Bangerth, M. Bergbauer, B. Blais, M. Fehling, R. Gassmöller, T. Heister, L. Heltai, M. Kronbichler, M. Maier, P.

Munch, S. Scheuerman, B. Turcksin, S. Uzunbajakau, D. Wells, and M. Wichrowski. deal.II software webpage. https://dealii.org/. 2025.

52. Barrett, A., J. A. Brown, M. A. Smith, A. Woodward, J. P. Vavalle, A. Kheradvar, B. E. Griffith, and A. L. Fogelson. A model of fluid-structure and biochemical interactions for applications to subclinical leaflet thrombosis. *Int. J. Numer. Meth. Biomed. Eng.* 39(5):e3700, 2023.
53. Brown, J. A., J. H. Lee, M. A. Smith, D. R. Wells, A. Barrett, C. Puelz, J. P. Vavalle, and B. E. Griffith. Patient-Specific Immersed Finite Element-Difference Model of Transcatheter Aortic Valve Replacement. *Ann. Biomed. Eng.* 51(1):103–116, 2023.
54. Davey, M., C. Puelz, S. Rossi, M. A. Smith, D. R. Wells, G. M. Sturgeon, W. P. Segars, J. P. Vavalle, C. S. Peskin, and B. E. Griffith. Simulating cardiac fluid dynamics in the human heart. *PNAS Nexus*. 3(10):pgae392, 2024.
55. Noether, G. E. Sample size determination for some common nonparametric tests. *J. Am. Stat. Assoc.* 82(398):645–647, 1987.
56. Elbaz, M. S. M., R. J. van der Geest, E. E. Calkoen, A. de Roos, B. P. F. Lelieveldt, A. A. W. Roest, and J. J. M. Westenberg. Assessment of viscous energy loss and the association with three-dimensional vortex ring formation in left ventricular inflow: In vivo evaluation using four-dimensional flow MRI. *Magn. Reson. Med.* 77(2):794–805, 2017.
57. Faggiano, A., B. Rocca, C. Y. Shim, S. Farhud, G. R. Hong, N. Gaibazzi, P. Faggiano, G. Benfari, S. Qamruddin, A. Kheradvar, and G. S. Pressman. Clinical and hemodynamic implications of mitral annular calcification. *J. Heart Valve Soc.* 2(2):182–197, 2025.
58. Reddy, Y. N. V., J. P. Murgo, and R. A. Nishimura. Complexity of defining severe "stenosis" from mitral annular calcification. *Circulation.* 140(7):523–525, 2019.
59. Guerrero, M. E., M. F. Eleid, D. D. Wang, A. Pursnani, S. K. Kodali, I. George, I. Palacios, H. Russell, R. R. Makkar, S. Kar, L. F. Satler, V. Rajagopal, G. Dangas, G. H. L. Tang, J. M. McCabe, B. K. Whisenant, K. Fang, P. Balan, R. Smalling, T. Kaptzan, B. Lewis, P. S. Douglas, R. T. Hahn, J. Thaden, J. K. Oh, M. Leon, W. O'Neill, and C. Rihal. 5-year prospective evaluation of mitral valve-in-valve, valve-in-ring, and valve-in-MAC outcomes: MITRAL trial final results. *JACC Cardiovasc. Interv.* 16(18):2211–2227, 2023.

Publisher's Note Springer Nature remains neutral with regard to jurisdictional claims in published maps and institutional affiliations.